FULL PAPER

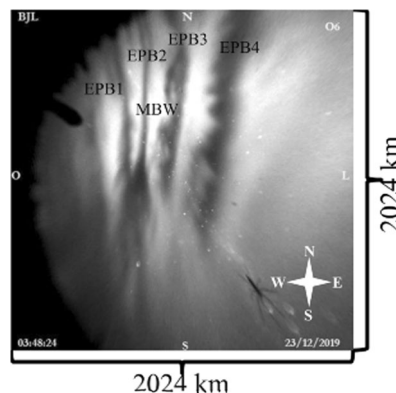**Open Access**

Secondary instability generated on the equatorial plasma bubbles wall due to an interaction with midnight brightness wave

Cosme Alexandre Oliveira Barros Figueiredo[1*] , Rodrigo A. Miranda[2], Cristiano Max Wrasse[1], Hisao Takahashi[1], Diego Barros[1], Fábio Egito[3], Geângelo de Matos Rosa[4] and Antonio Hélder Rodrigues Sampaio[4]

Abstract

Interaction between Equatorial Plasma Bubbles (EPBs) and midnight Brightness wave (MBW) was observed over Bom Jesus da Lapa (13.3° S, 43.5° W; Quasi-Dipole geomagnetic latitude of 14.1° S), using OI 630 nm all-sky images. On the night of December 22nd, 2019, an EPB was seen propagating eastward in its fossil stage until it interacted with an MBW. After the interaction, the west walls of EPBs generated secondary instabilities that can be associated with gradient drift instability (GDI) and/or Kelvin–Helmholtz instabilities (KHI). We suggest that the MBW contributed to generate a shear in the EPBs walls due to changes in the thermospheric dynamics, such as neutral wind in the F layer height. Furthermore, spectral analysis of the all-sky images suggests that GDI and/or KHI generated turbulence and helped to dissipate the EPBs.

Graphical Abstract

*Correspondence:
Cosme Alexandre Oliveira Barros Figueiredo
anagetinga@gmail.com
Full list of author information is available at the end of the article

Figueiredo *et al. Earth, Planets and Space* (2023) 75:141

Page 2 of 9

Introduction

In the equatorial ionosphere, several geophysical phenomena occur; the main phenomena are called Equatorial plasma bubbles (EPBs). EPBs are frequently observed from September to April over South America. They typically drift eastward with speeds ranging from 50 to 200 m/s and a latitudinal dimension from hundreds to thousands of kilometers (e.g., Barros et al. 2018). Also, EPBs are plasma depletions generated by Rayleigh–Taylor instability in the equatorial ionosphere's bottom side (Abdu 2001). The gravitational force and density gradient are antiparallel in the F-layer bottom-side, resulting in Rayleigh–Taylor instability (Haerendel 1973; Kelley 2009). In addition, EPB generates scintillations on the electromagnetic signals that can reduce the accuracy of GNSS signals or even disable them in extreme cases resulting in effects on social life highly dependent on technology. Much research has been conducted in recent decades forecasting of EPBs to reduce the impact of these anomalies on society (Takahashi et al. 2016).

In the equatorial thermosphere, the neutral temperature tends to decrease along the night. However, on some days, the neutral temperature increases near midnight. This phenomenon in the neutral temperature is known as midnight temperature maximum (MTM) (e.g., Herrero et al. 1993; Figueiredo et al. 2017; Mesquita et al. 2018 and references therein). The MTM causes a large increase in neutral temperature during the summer solstice (DJF). In addition, it changes the direction of the meridional wind from equatorward to poleward (Herrero et al. 1993; Meriwether et al. 2011). As a result of the poleward wind, the F layer moves downward along the magnetic field lines, consequently, the intensity of the OI 630 nm emission increase (Link and Cogger 1988). Moreover, Akmaev et al. (2010) showed that the MTM typically leads the Midnight neutral Density Maximum (MDM), whereby the MDM occurs above the MTM at the same longitude or lagging eastward of the MTM at the same height. Finally, when the MTM is observed in all-sky images, it is called a midnight brightness wave (MBW), and it propagates poleward in both hemispheres (e.g., Colerico et al. 1996).

Despite EPB and MBW being equatorial phenomena that frequently happen in the ionosphere and thermosphere; however, their interaction is rare. In the literature, we find only a pre-printed (Figueiredo et al. 2020) and peer-reviewed papers (Hickey and Martinis 2020) about EPB and MBW interaction. Hickey and Martinis (2020) observed an event in that MBW modified the EPB depletion, and the EPB structure became brighter than the ambient. Based on numerical simulation by Krall et al. (2009), Hickey and Martinis (2020) suggest that a poleward meridional wind and a converging zonal wind

generated by MBW/MTM can turn an EPB into a brightness structure.

This work aims to describe and discuss the interaction between EPBs and an MBW that generated secondary instabilities on the west walls EPBs over Bom Jesus da Lapa observatory, Brazil, using OI 630.0 nm airglow imaging. The following sections will provide details about the interaction and a possible explanation.

Instrumentation and methodology

In December 2019, the National Institute for Space Research (INPE) and the Federal Institute of Education, Science and Technology Baiano (IF Baiano) collaborated to build a new airglow observatory at Bom Jesus da Lapa (BJL) (Wrasse et al. 2021), located at 13.3° S, 43.5° W (Quasi-Dipole geomagnetic latitude of 14.1° S). Figure 1 shows the observatory's location, marked by a black circle in the center. The magnetic equator at 250 km altitude is shown as a black line, while red lines represent magnetic field lines and quasi-dipole latitudes. The all-sky imager at the BJL observatory measures airglow emissions from the mesosphere to the thermosphere. This observatory provides good coverage of the area under the Equatorial Ionization Anomaly (EIA) South crest, making it an ideal location for monitoring the dynamics of the ionosphere and thermosphere.

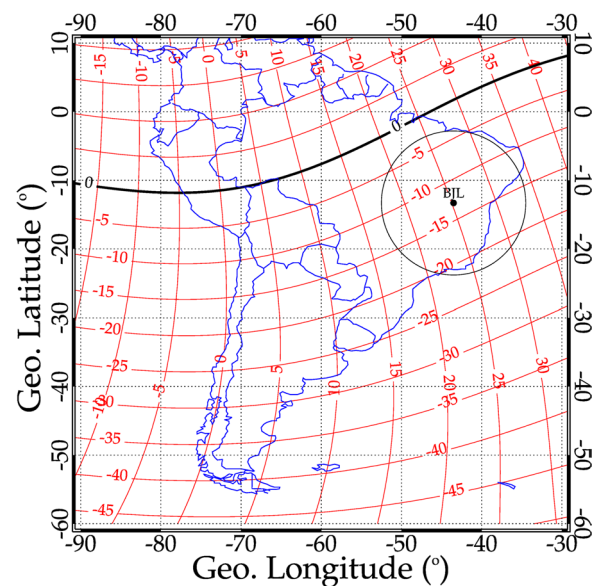**Fig. 1** The airglow observatory at Bom Jesus da Lapa, Brazil, is represented by a black dot in the center of the black circle. The black circle denotes the field of view of the all-sky imager for the OI 630 nm emission, which has a radius of 9°. The black line shows the magnetic equator at 250 km altitude, while the magnetic field lines and quasi-dipole latitudes are represented by the red lines

Figueiredo *et al. Earth, Planets and Space*   (2023) 75:141

Page 3 of 9

The all-sky imager at the BJL observatory is a versatile instrument that can be used to measure a variety of airglow emissions. The imager has a 180° field of view fisheye lens, a 3-inch diameter interference filter, a telecentric lens system, and a 1024×1024 pixels array CCD camera. The imager measures the following airglow emissions: Hydroxyl (715–930 nm) with 15 s of image integration; OI 557.7 nm, O_2, and OI 630.0 nm with 90 s of image integration. The imager is a valuable tool for studying the dynamics of the ionosphere and thermosphere. It can be used to track changes in airglow emissions over time, providing insights into the processes that are driving these changes.

Spectral analysis

We characterize the spectral properties of the secondary instability arising at EPB walls by computing the power spectrum of the relative intensity data from the unwarped images. Two different methods are described in this section. Consider a coordinate system in which the X direction corresponds to the West–East direction and the Y direction corresponds to the South-North direction. Let $I(x, y, t)$ denote the intensity at position (x, y), at time t. The one-dimensional spatial Fourier transform of I along the Y direction for a fixed value of x can be written as

$$\hat{I}(x, k_y, t) = \frac{1}{N_y} \sum_{y=0}^{N_y-1} I(x, y, t) e^{ik_y y}, \tag{1}$$

where k_y represents the wavenumber in the Y direction, $i = \sqrt{-1}$, and the (^) denotes a complex quantity. The power spectrum PS along the Y direction is given by

$$PS(x, k_y, t) = \left| \hat{I}(x, k_y, t) \right|^2. \tag{2}$$

Similar expressions for Eqs. (1) and (2) can be written for the Fourier transform of I and the power spectrum along the X direction, for fixed y and t.

Since the EPBs are generally not aligned with the Y direction in the unwarped images, Eq. (1) can be rewritten for an arbitrary line path $s(t)$ as follows. Let $I(s, t)$ be the intensity data along s at time t. The Fourier transform of I can be written as

$$\hat{I}(k_s, t) = \frac{1}{N_s} \sum_{s=0}^{N_s-1} I(s, t) e^{ik_s s}, \tag{3}$$

where N_s represents the number of points along s, and k_s is the wavenumber along s. Therefore, the power spectrum can be obtained by

$$PS(k_s, t) = \left| \hat{I}(k_s, t) \right|^2. \tag{4}$$

The development of secondary instabilities at the EPB wall can be analyzed with a spectrogram constructed by plotting $PS(k_s, t)$ as a function of both k_s and t. Note that the path $s(t)$ must be set to a straight line, parallel to an EPB and intersecting the EPB wall contour. Moreover, the path $s(t)$ must be carefully defined for each image to ensure that $s(t)$ "follows" the drift of the EPB wall at the same position relative to the wall contour. Since EPB walls can be tilted from the geographic meridian as they drift, the path $s(t)$ will deviate from the pixel alignment of the airglow images. To maintain the spatial resolution along $s(t)$ the same at different times, we carefully measure the length of $s(t)$ and keep it constant within all unwarped images. Since each pixel in the unwarped images represent the same spatial scale (3 km), the length of the path $s(t)$ will also represent a constant spatial scale for all images. Then, we divide $s(t)$ into a set of equidistant points, and obtain the intensity $I(s, t)$ at each point along $s(t)$ by applying a bilinear interpolation. This ensures that the set of spatial scales and wavenumbers is the same for all images, even after the EPB wall becomes tilted due to the drift.

The power spectrum of the intensity images at the EPB walls can also be computed by taking the average of $PS(x, k_y, t)$ over x, around the wall contour. The x-averaged power spectrum PS_x can be defined by

$$PS_x(k_y, t) = \left\langle PS(x, k_y, t) \right\rangle_x = \frac{1}{x_f - x_i} \sum_{x=x_i}^{x_f} \left| \hat{I}(x, k_y, t) \right|^2, \tag{5}$$

where x_i and x_f represent the initial and final values of x over which the average is computed. The Fourier transforms of Eqs. (1) and (3) are computed using the fast Fourier transform (FFT) algorithm. The FFT and the bilinear interpolation algorithms employed in this paper are implemented on the GNU Octave program (Eaton 2012).

Results and discussion

On the night of December 22nd, 2019, Fig. 2 shows the original (panel I) and unwarped (panel II) $(2024 \times 2024 \ km^2)$ OI 630.0 nm relative intensity images taken at the BJL observatory. It is important to note that the geomagnetic conditions were quiet (Kp ≤ 3). Between 03:30 UT and 04:09 UT (Local time = UT − 3 h), we observed four EPBs, marked as B1, B2, B3, and B4, moving eastward in Fig. 2. In addition, the zonal drift speed of the EPB was 49 ± 5 m/s. The zonal drift speed was calculated using a 2-D Fourier Transform (Wrasse et al. 2007). Furthermore, EPBs after local midnight are normally called fossil plasmas bubbles. They are frequently used
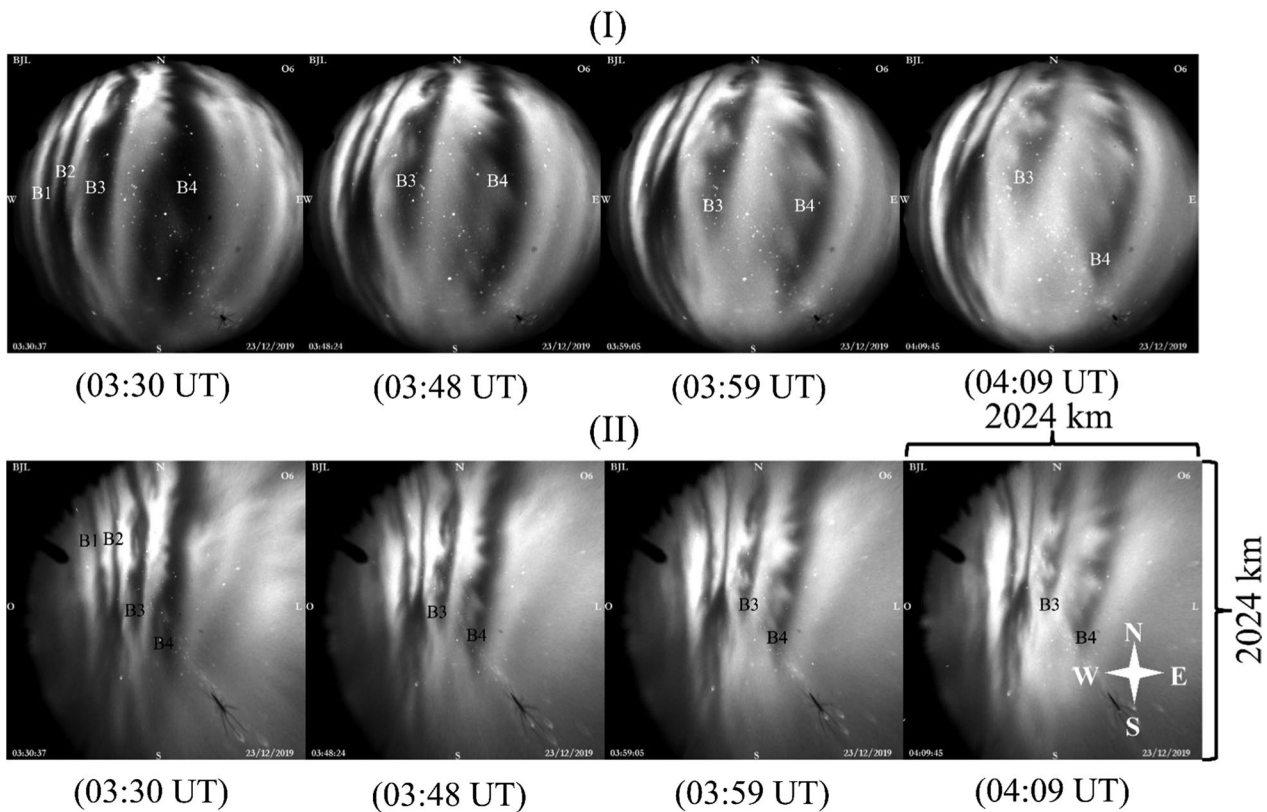
Figueiredo *et al. Earth, Planets and Space*   (2023) 75:141

Page 4 of 9

Fig. 2 OI 630 nm original (**I**) and unwarped (**II**) images taken from Bom Jesus da Lapa observatory on the night of December 22nd, 2019, between 03:30 and 04:09 UT (LT = UT − 3 h) show the interaction between EPB and MBW. The interaction generated GDI and/or KHI on the west wall of the EPB B3 and oscillation structures on EPB B4. The letters and numbers, B1, B2, B3, and B4 are the EPB's identification

as background ionosphere motion tracers because they move with the ambient plasma (e.g., Sobral et al. 2009).

Moreover, secondary structures were generated on the west wall of EPB B3 and B4. At the same time, a bright region was observed propagating southwestward in the top images. Colerico et al. (1996) observed bright structures propagating southward over Arequipa, Peru, using an all-sky imager. They called this phenomenon a midnight brightness wave (MBW). The MBW is an optical phenomenon generated by the downward movement of the F layer due to the midnight temperature maximum. The MTM increases the neutral temperature and changes the neutral wind direction near midnight. This has been observed by other researchers, such as Herrero et al. (1993), Meriwether et al. (2011), and Figueiredo et al. (2017). Using the zonal and meridional keograms of the images, we calculated the speed of the meridional movement of the MBW, which is 166 ± 19 m/s. An animation with OI 630.0 nm images of Fig. 2 is presented in Additional file 1: Movie S1.

Hickey and Martinis (2020) observed an interesting interaction between EPB and MBW. The authors observed a bright zone on the EPB walls. They suggested

that bright intensification in the EPB walls is due to changes in the neutral wind caused by the MBW. On the other hand, our present observation showed an MBW and an EPB interacting. We do not observe the brightness of the EPBs wall, but secondary instabilities on the west EPB wall.

Figure 2 shows the development of billows associated with secondary instability on the west wall of EPB B3 during the interaction between EPBs and an MBW. The first billow grows at 03:30 UT with 28 km wide and 324 km latitudinal length. At 03:48 UT, the second billow appears. At 04:09 UT, the EPB B3 starts to dissipate, but the billows still grow with 60 km wide and 412 km latitudinal length, i.e., increase the distance themselves. On the other hand, EPB B4 shows oscillatory characteristics on the west wall, but it does not develop to billows as EPB B3. We calculated the fluctuations distance on EPB B4 at 03:48 UT and found an oscillation with a length of ~ 139 km.

Regarding the secondary instability that appears on the west wall of EPB B3 and B4, Tsunoda (1983) suggested that the western wall is more favorable for the onset of wind-driven secondary instabilities because the

nighttime thermospheric zonal neutral wind blows eastward in the opposite direction as the zonal plasma density gradient. However, Yokoyama et al. (2015) showed via a high-resolution plasma bubble model that a vertical shear of zonal plasma drift velocity at the bottom side of the F layer plays a key role in speeding instability growth at the west wall and causing EPBs east–west asymmetry. Also, it has been discussed that a shear instability mechanism plays a crucial role in seeding the EPBs (Hysell and Kudeki 2004; Hysell et al. 2005; Aveiro and Hysell 2010).

Behnke and Harper (1973) and Harper (1973) observed that the MTM reversal the thermospheric meridional wind component, consequently, causes the drop in the F layer. Herrero et al. (1993) showed that a simple meridional wind abatement is all that is required for the F layer collapse to occur (e.g., see results of Figueiredo et al. (2017)). Based on our observations, we suggest that the plasma density descending along the magnetic field lines and EPB B3/B4 receding along the same lines interact and may generate secondary instabilities on the west wall of EPB.

Based on the secondary instabilities observed in the plasma bubbles, we can suggest two possibilities: gradient drift instability and/or Kelvin Helmholtz instabilities. Rathod et al. (2021) and references therein state that the F region is a transition region where the collision frequency is weak enough to allow GDI and KHI to grow. To grow the GDI, it is necessary for the $\mathbf{E} \times \mathbf{B}$ drift to have a component moving in the same direction as the plasma density gradient. On the other hand, KHI is hydrodynamics instability that is generated by the velocity shear interface. In the ionosphere, these plasma irregularities are important to produce turbulence.

We compute the power spectrum of the relative intensity along a line path (Eq. 4) located on the west wall of EPBs B3 and B4, over the interval from 02:40:49 UT to 04:20:25 UT, which gives a sequence of 21 images. Figure 3a, b show the spectrograms of EPB B4 and B3 as a function of the wavenumber k and time t (a sequential number). Also, the energy is represented by a color scale. Figure 3a shows that most of the energy is contained in low-k modes. From 03:27:04 UT to 04:13:18 UT (corresponding to the interval [14, 28] in the x-axis of Fig. 3a), a red patch marked by an arrow can be observed going from $k \sim 0.008$ to $k \sim 0.005$. This means that energy is transferring from high-k to low-k, which is related to the growth of structures on the west wall of EPB B4.

The spectrogram of Fig. 3b also shows that most of the energy is contained in low-k modes. However, the dark red area clearly spreads toward higher-k as the time increases, which suggests that energy is being transferred to higher wavenumbers. This might be related to the instability breaking observed in the west wall of EPB
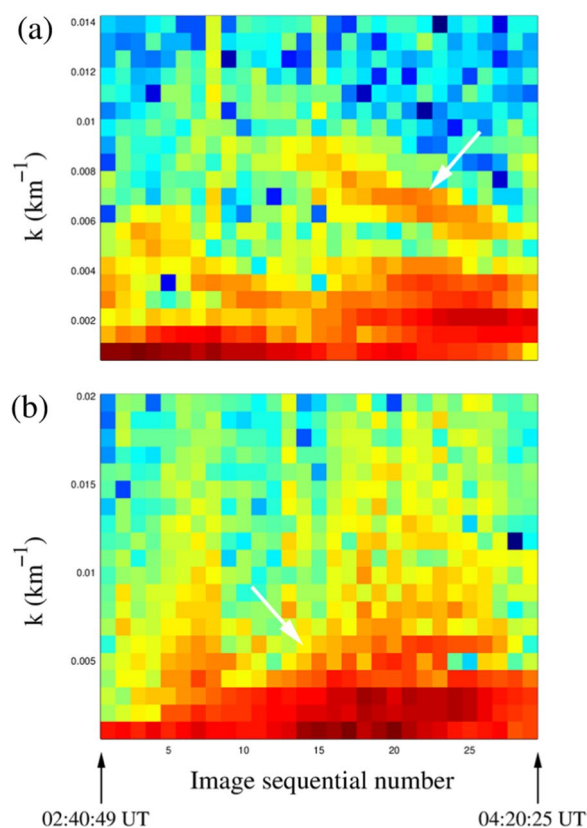

Fig. 3 **a** Spectrogram obtained from the sequence of 29 "slices" at EPB B4. A white arrow indicates the spectral signature of the oscillations due to the growth of the GDI. **b** Spectrogram obtained from the sequence of "slices" at EPB B3. The white arrow indicates the spectral signature of the energy cascade due to turbulence generation

B3. Whereby, we suggest that the MTM/MBW passage increases the collisional frequency in low altitudes and low geomagnetic latitudes in the F region due to the increases in the neutral density. Furthermore, the MBW reversed the neutral wind from its original direction (equatorward) to poleward, causing, the F layer abatement from high to low altitude along the magnetic field lines. This result enhances the local vertical electron density gradient, generating a vertical gradient polarization electric field. So, this environment might be enough to trigger the GDI on the west wall of EPB B4. Conversely, it might be possible that EPB B3 developed the KHI due to the higher background velocity shear between MBW and EPB B3 along the magnetic field lines.

Huba et al. (1988) performed a numerical simulation to investigate the KHI both with and without magnetic-ionospheric coupling in high latitudes. The authors observed that ionospheric coupling (collisional effects) influences the KHI such as slowing its expansion and suppressing vortex formation. Keskinen et al. (1988) performed

Figueiredo *et al. Earth, Planets and Space* (2023) 75:141

Page 6 of 9

a nonlinear numerical simulation of KHI both with and without Pedersen conductivity coupling in high latitudes. Keskinen et al. (1988) concluded that KHI with neutral wind, density gradient, and Pedersen conductivity induce (1) an increased time scale for Kelvin–Helmholtz instability wave growth; (2) inhibit Kelvin–Helmholtz vortex formation; (3) lead to nonlinear structures; (4) generate small scale turbulence. Therefore, in summary, the KHI can develop vortices that can break and spread energy towards smaller scales, leading to an energy cascade and turbulence (Huba et al. 1988; Keskinen et al. 1988).

Next, we analyze the ionospheric turbulence caused by the breakdown of KHI vortices on the west wall of EPB B3. We compute the *x*-averaged power spectrum PS_x (Eq. 5) of the intensity data within the black rectangles displayed in Fig. 4a, b, for the unwarped images at 03:51:58 UT and 04:13:18 UT, respectively. The rectangles cover the billows structures seen at the west walls of

B3. Figure 4c displays PS_x of the selected intensity data in Fig. 4a. The black arrow points to the characteristic scale of the KHI vortices in the north–south direction. The power spectrum follows a power-law $PS_x (k_y) \sim k_y^{-n}$ with a spectral index of $n = 2.68 \pm 0.22$, computed within the interval [0.005, 0.02]. This spectral index is close to values from observational (e.g., Chian et al. 2018) and numerical (e.g., Huba et al. 1988) studies. Figure 4d shows the PS_x of the selected region in Fig. 4b. In this figure, the spectral index is equal to -1.76, indicating that the spectral index has decreased over time, which can result in more energy transfer from the KHI scale toward smaller scales, due to KHI wave breaking.

Rino et al. (2018, 2023) studied how the spectral density of EPBs varies over time. They reported that the spectral density rises in the growth phase of EPBs and falls in the decay phase, changing the power-law exponent from ~ 3 to ~ 2. They also suggested that the background plasma
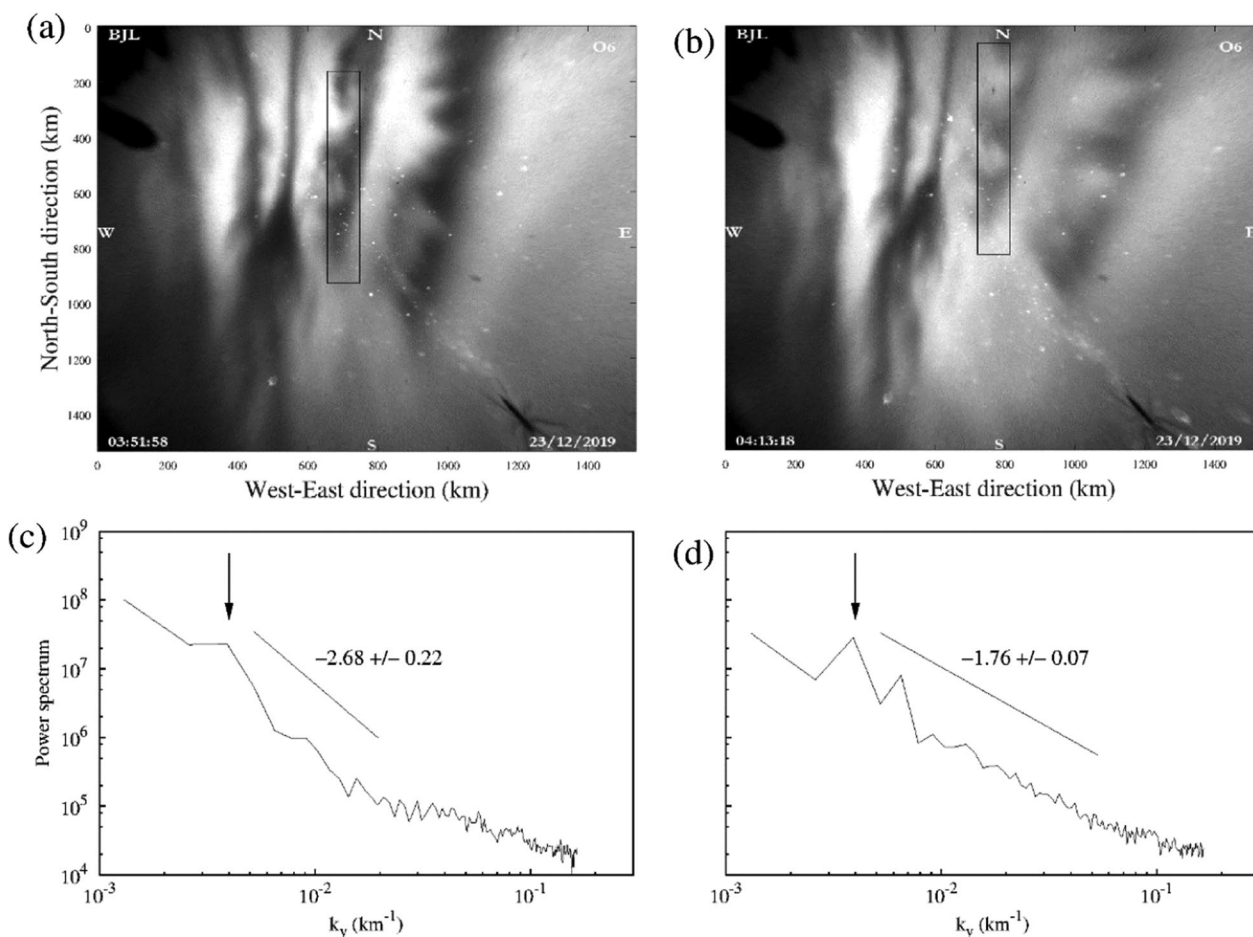

Fig. 4 **a** Unwarped image taken at 03:51:58 UT. The black rectangle indicates the selected region of the EPB B3 for spectrum analysis. **b** Unwarped image taken at 04:13:18 UT, and selected region for spectrum analysis. **c** Power spectrum $PS_x(k_y)$ for the selected region of the EPB B3 at 03:51:58 UT. **d** Power spectrum $PS_x(k_y)$ for the selected region of the EPB B3 at 04:13:18 UT. Black arrows indicate the north–south characteristic scale of the KHI vortices. Black continuous lines indicate the spectral slope

Figueiredo *et al. Earth, Planets and Space*   (2023) 75:141

Page 7 of 9

turbulence may influence the spectral density of EPBs. Our observations support their findings, as shown in Fig. 4c, d. The spectral density of EPB B3 follows a power-law distribution with an exponent decreasing from 2.68 to 1.76, which agrees with the simulation results of Rino et al. (2023, Fig. 6).

Regarding Fig. 4d, we find that $PS(k_y) \sim k_y^{-n}$ with $n = 1.76 \pm 0.7$ at 04:13 UT. Huba et al. (1988) applied the power spectrum to their numerical simulations results of the KHI with a collisional regime and found that $PS(k_x) = k_x^{-n}$ with $n = 1.9 \pm 0.5$ and $PS(k_y) = k_y^{-n}$ with $n = 1.6 \pm 0.5$ at a late time ($t = 56$ s.). In addition, according to Basu et al. (1988), the $PS(k_y) = k_y^{-n}$ with n within the interval [1.7, 2] in the direction of velocity shear. Our present results agree with Huba et al. (1988) and Basu et al. (1988).

Huba et al. (1988) explained that the suppression of large-scale vortices in the ionosphere (i.e., in the collisional regime) is thought to be the cause of the "shallowing" of the spectrum. Also, the authors point out that in the long-wavelength regime, i.e., at small wavenumber k, the large-scale vortices contain significant power. If these vortices do not emerge (as they do in the collisional regime), the power at small k decreases, resulting in a reduced power spectrum. Therefore, our observational results agree with the numerical simulation of KHI made by Huba et al. (1988). In addition, as observed in Figs. 3 and 4, EPB B3 and B4 dissipate faster than EPB B1 and B2. Therefore, the KHI generated on the west EPB B3 can lead to the development of vortices that can break and spread energy towards smaller scales, leading to an energy cascade and turbulence.

A limitation of our study is the lack of in situ plasma density gradient and neutral wind data. These data could provide further insights into the interaction between EPB and MBW, triggering KHI and GDI to advance the discussions. Therefore, we recommend further observations with multi-instruments and numerical simulations to investigate this kind of interaction and its effect on generating secondary instabilities on the EPB wall.

Summary

On the night of December 22nd, 2019, at the Bom Jesus da Lapa airglow observatory in Brazil, we observed an interesting interaction between the Equatorial Plasma Bubbles (EPBs) and a Midnight Brightness Wave (MBW). The EPBs were moving eastward in an apparent fossil stage until they interacted with an MBW. This interaction triggered Kelvin Helmholtz Instability (KHI) and/or Gradient Drift Instability (GDI) on the west walls of the EPBs. Contrary to previous literature, we found that the MBW did not enrich the EPB wall with plasma. Instead, it generated vortices that broke and dispersed energy to smaller scales. The process of KHI and GDI leads to an energy cascade and turbulence generating an environment to the EPBs dissipate.

In this paper, the spectral properties of the turbulence induced by the breakdown of KHI vortices were characterized. The power spectra computed from intensity images displayed power laws with spectral slopes varying from -2.68 to -1.76. The latter value is similar to the $-5/3$ spectral index obtained in fluid experiments and the Kolmogorov 1941 theory of hydrodynamic turbulence (Frisch 1995). The $-5/3$ slope of power spectra has been also widely reported from observational data in turbulent plasmas, for example, the solar wind (Matthaeus et al. 1982; Leamon et al. 1998; Bruno and Carbone 2005; Narita et al. 2006; Chian and Miranda 2009; Miranda et al. 2021). In magnetohydrodynamic (MHD) turbulence, the slope $-3/2$ has been reported in agreement with the Iroshnikov-Kraichnan theory of MHD turbulence (Biskamp and Schwarz 2001). However, the mechanisms leading to these spectral slopes can be very different in the ionosphere. For example, Chian et al. (2018) showed that the spectral slope of ionospheric turbulence in the presence of EPBs can be close to -2.3 in the bottomside F-region, and close to $-5/3$ in the peak F-region. A careful analysis of the spectral slopes obtained in this paper will be the topic of a future work.

Supplementary Information

The online version contains supplementary material available at https://doi.org/10.1186/s40623-023-01892-7.

Additional file 1: Movie S1. On the night of December 22, 2019, between 02:00 and 05:31 UT (LT = UT - 3 h). The movie contains 630 nm unwarped images covering an area of 2024 x 2024 km^2 at 250 km altitude. It showed an interaction between EPB and MBW, creating GDI and/or KHI on the west wall of the second EPB from the right-hand side. Furthermore, oscillation structures were observed on the first EPB on the right-hand side.

Figueiredo *et al. Earth, Planets and Space*   (2023) 75:141

Page 8 of 9

Author details

[1]Space Weather Division, National Institute for Space Research (INPE), São José dos Campos, Brazil. [2]University of Brasilia, UnB-Gama Campus and Institute of Physics, Brasília, DF 70910-900, Brazil. [3]Federal University of Campina Grande (UFCG), Campina Grande, Brazil. [4]Federal Institute for Education, Science and Technology Baiano (IF Baiano), Bom Jesus da Lapa, Brazil.

References

Abdu MA (2001) Outstanding problems in the equatorial ionosphere–thermosphere electrodynamics relevant to spread F. J Atmos Sol Terr Phys 63(9):869–884. https://doi.org/10.1016/S1364-6826(00)00201-7

Akmaev RA, Wu F, Fuller-Rowell TJ, Wang H, Iredell MD (2010) Midnight density and temperature maxima, and thermospheric dynamics in Whole Atmosphere Model simulations. J Geophy Res Space Phy 115(A8). https://doi.org/10.1029/2010JA015651

Aveiro HC, Hysell DL (2010) Three-dimensional numerical simulation of equatorial F region plasma irregularities with bottomside shear flow. J Geophys Res 115:A11321. https://doi.org/10.1029/2010JA015602

Barros D, Takahashi H, Wrasse CM, Figueiredo CAOB (2018) Characteristics of equatorial plasma bubbles observed by TEC map based on ground-based GNSS receivers over South America. Ann Geophys 36(1):91–100. https://doi.org/10.5194/angeo-36-91-2018

Basu S, Basu S, MacKenzie E, Fougere PF, Coley WR, Maynard NC, Winningham JD, Sugiura M, Hanson WB, Hoegy WR (1988) Simultaneous density and electric field fluctuation spectra associated with velocity shears in the auroral oval. J Geophys Res 93(A1):115–136. https://doi.org/10.1029/JA093iA01p00115

Behnke RA, Harper RM (1973) Vector measurements of F region ion transport at Arecibo. J Geophys Res 78:8222–8234

Biskamp D, Schwarz E (2001) On two-dimensional magnetohydrodynamic turbulence. Phys Plasmas 8(7):3282–3292

Bruno R, Carbone V (2005) The solar wind as a turbulence laboratory. Living Rev Sol Phys 2:4

Chian AC-L, Miranda RA (2009) Cluster and ACE observations of phase synchronization inintermittent magnetic field turbulence: a comparative study of shocked and unshockedsolar wind. Ann Geophys 27:1789–1801

Chian AC-L et al (2018) Multi-spectral optical imaging of the spatiotemporal dynamics of ionospheric intermittent turbulence. Sci Rep 8:10568

Colerico M, Mendillo M, Nottingham D, Baumgardner J, Meriwether J, Mirick J, Reinisch B, Scali J, Fesen C, Biondi M (1996) Coordinated measurements of F region dynamics related to the thermospheric midnight temperature maximum. J Geophys Res Space 101:26783–26793

Eaton JW (2012) GNU Octave and reproducible research. J Process Control 22(8):1433–1438

Figueiredo CAOB, Buriti RA, Paulino I, Meriwether JW, Makela JJ, Batista IS, Barros D, Medeiros AF (2017) Effects of the midnight temperature maximum observed in the thermosphere–ionosphere over the northeast of Brazil. Ann Geophys 35:953–963. https://doi.org/10.5194/angeo-35-953-2017

Figueiredo CA, Wrasse CM, Takahashi H, Otsuka Y, Shiokawa K, Buriti RA, Paulino I, Barros D (2020) Observational evidence of interaction between equatorial plasma bubble, medium-scale traveling ionospheric disturbances, and midnight brightness wave at low latitudes. Authorea. https://doi.org/10.1002/essoar.10503764.1

Frisch U (1995) Turbulence: the legacy of AN Kolmogorov. Cambridge University Press, Cambridge

Haerendel G (1973) Theory of equatorial spread-F, report Max-Planck Institute

Harper R (1973) Nighttime meridional neutral winds near 350 km at low to mid-latitudes. J Atmos Terr Phys 35:2023–2034

Herrero F, Spencer N, Mayr H (1993) Thermosphere and F-region plasma dynamics in the equatorial region. Adv Space Res 13:201–220

Hickey DA, Martinis C (2020) All-sky imaging observations of the interaction between the brightness wave and ESF airglow depletions. J Geophys Res Space Phys 125:e2019JA027232. https://doi.org/10.1029/2019JA027232

Huba JD, Mitchell HG, Keskinen MJ, Fedder JA, Satyanarayana P, Zalesak ST (1988) Simulations of plasma structure evolution in the high-latitude ionosphere. Radio Sci 23(4):503–512. https://doi.org/10.1029/RS023i004p00503

Hysell DL, Kudeki E (2004) Collisional shear instability in the equatorial F region. J Geophys Res 109:A11301. https://doi.org/10.1029/2004JA010636

Hysell DL, Kudeki E, Chau JL (2005) Possible ionospheric preconditioning by shear flow leading to equatorial spread F. Ann Geophys 23:2647–2655

Kelley MC (2009) The earth's ionosphere. Elsevier, Amsterdam

Keskinen MJ, Mitchell HG, Fedder JA, Satyanarayana P, Zalesak ST, Huba JD (1988) Nonlinear evolution of the Kelvin–Helmholtz instability in the high-latitude ionosphere. J Geophys Res 93(A1):137–152. https://doi.org/10.1029/JA093iA01p00137

Krall J, Huba J, Martinis C (2009) Three-dimensional modeling of equatorial spread F airglow enhancements. Geophys Res Lett 36:L10103. https://doi.org/10.1029/2009GL038441

Leamon RJ, Smith CW, Ness NF, Matthaeus WH (1998) Observational constraints on the dynamics of the interplanetary magnetic field dissipation range. J Geophys Res 103:4475–4787

Link R, Cogger L (1988) A reexamination of the OI 6300 Å nightglow. J Geophys Res Space 93:9883–9892

Matthaeus WH, Goldstein ML, Smith C (1982) Evaluation of magnetic helicity in homogeneous turbulence. Phys Rev Lett 48:1256–1259

Meriwether J, Makela J, Huang Y, Fisher D, Buriti R, Medeiros A, Takahashi H (2011) Climatology of the nighttime equatorial thermospheric winds and temperatures over Brazil near solar minimum. J Geophys Res Space 116:A04322. https://doi.org/10.1029/2011JA016477

Mesquita RL, Meriwether JW, Makela JJ, Fisher DJ, Harding BJ, Sanders SC, Tesema F, Ridley AJ (2018) New results on the mid-latitude midnight temperature maximum. Annales Geophysicae 36(2):541–553. https://doi.org/10.5194/angeo-36-541-2018

Miranda RA et al (2021) Complexity of magnetic-field turbulence at reconnection exhausts in the solar wind at 1 au. Astrophys J 923(2):132

Narita Y, Glassmeier K-H, Treumann RA (2006) Wave-number spectra and intermittency in the terrestrial foreshock region. Phys Rev Lett 97:191101

Rathod C, Srinivasan B, Scales W (2021) Modeling the dominance of the gradient drift or Kelvin–Helmholtz instability in sheared ionospheric E×B flows. Phys Plasmas 28(5):052903

Rino C et al (2018) Dynamic spectral characteristics of high-resolution simulated equatorial plasma bubbles. Prog Earth Planet Sci 5:83. https://doi.org/10.1186/s40645-018-0243-0

Rino C et al (2023) A three-dimensional stochastic structure model derived from high-resolution isolated equatorial plasma bubble simulation. Earth Planets Space 75:64. https://doi.org/10.1186/s40623-023-01823-6

Sobral JHA, Abdu MA, Pedersen TR, Castilho VM, Arruda DCS, Muella MTAH, Batista IS, Mascarenhas M, de Paula ER, Kintner PM, Kherani EA, Medeiros AF, Buriti RA, Takahashi H, Schuch NJ, Denardini CM, Zamlutti CJ, Pimenta AA, de Souza JR, Bertoni FCP (2009) Ionospheric zonal velocities at conjugate points over Brazil during the Copex campaign: experimental observations and theoretical validations. J Geophys Res Space Phys 114(A4):A04309. https://doi.org/10.1029/2008JA013896

Takahashi H, Wrasse CM, Denardini CM, Pádua MB, de Paula ER, Costa SMA, Otsuka Y, Shiokawa K, Galera Monico JF, Ivo A, Sant'Anna N (2016) Ionospheric TEC weather map over South America. Space Weather 14(11):937–949. https://doi.org/10.1002/2016SW001474

Figueiredo *et al. Earth, Planets and Space*   (2023) 75:141

Page 9 of 9

Tsunoda RT (1983) On the generation and growth of equatorial backscatter plumes: 2. Structuring of the west walls of upwellings. J Geophys Res 88:4869–4874

Wrasse CM, Takahashi H, Medeiros AF, Lima LM, Taylor MJ, Gobbi D, Fechine J (2007) Determinação dos parâmetros de ondas de gravidade através da análise espectral de imagens de aeroluminescência. Revista Brasileira De Geofísica 25(3):257–265. https://doi.org/10.1590/S0102-261X2007000300003

Wrasse CM, Figueiredo CAOB, Barros D, Takahashi H, Carrasco AJ, Vital LFR, Rezende LCA, Egito F, Rosa GM, Sampaio AHR (2021) Interaction between equatorial plasma bubbles and a medium-scale traveling ionospheric disturbance, observed by OI 630 nm airglow imaging at Bom Jesus de Lapa, Brazil. Earth Planet Phys 5(5):397–406. https://doi.org/10.26464/epp2021045

Yokoyama T, Jin H, Shinagawa H (2015) West wall structuring of equatorial plasma bubbles simulated by three-dimensional HIRB model. J Geophys Res Space Phys 120:8810–8816. https://doi.org/10.1002/2015JA021799

Publisher's Note